Fabrication of Nitrogen-Modified Annealed Nanodiamond with Improved Catalytic Activity

Yangming Lin[†,‡] and Dangsheng Su[‡,§,*]

[†]School of Chemistry and Materials Science, University of Science and Technology of China, Hefei 230001, People's Republic of China, [‡]Shenyang National Laboratory for Materials Science, Institute of Metal Research, Chinese Academy of Sciences, Shenyang 110016, People's Republic of China, and [§]Department of Inorganic Chemistry, Fritz Haber Institute of the Max Planck Society, Berlin 14195, Germany

ABSTRACT Annealed ultradispersed nanodiamond (ADD) with sp^2 curved concentric graphitic shells is an interesting hybrid material consisting of the remarkable surface properties of graphene-based nanomaterials and the intrinsic properties of a diamond core. In this case, based on its specific properties and surface oxygen functional groups, nitrogen-modified ADD powders have been tunably synthesized *via* three different preparation methods in a calcination treatment process. The detailed formation and dynamic behaviors of the nitrogen species on the modified ADD during the preparation process are revealed by elemental analysis, X-ray photoelectron spectroscopy (XPS) and temperature-programmed desorption. Moreover, we study the catalytic performance on the metal-free nitrogen-modified ADD catalysts by means of selective oxidation of benzylic alcohols as a probe reaction. The results indicate that the modified ADD catalysts exhibit a higher catalytic activity than pristine ADD. By correlating XPS data with catalytic measurements, we conclude that the pyridinic nitrogen species plays a pivotal role in the catalytic reaction. Our work provides valuable information on the design of modified carbon materials with more excellent properties.

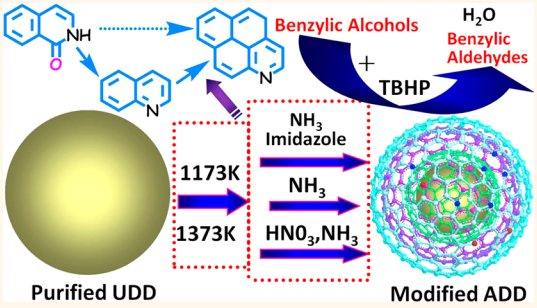

KEYWORDS: nanodiamond · metal-free catalysis · modification · selective oxidation · pyridinic nitrogen

Due to their unique properties, nanocarbon materials (*e.g.*, single/multiwalled carbon nanotube, nanographite, graphene, fullerene, and nanocone) have been widely studied for various possible applications.[1−7] The sp^3-bonded ultradispersed nanodiamond (UDD) as another kind of nanocarbon material has been used as biomaterials, nanocomposites, and fluorescent and tribology materials.[8−13] Theoretical calculation indicated that bare UDD presented thermodynamic stability and did not form larger grains in a broad range of pressures and temperatures, even the particle size was reduced to about 3 ± 1 nm.[14] Recently, the annealing graphitization of UDD in an inert atmosphere or in vacuum (T > 1200 °C) has attracted increasing attention due to the formation of onion-like carbon, which is a fascinating non-planar-related material with multiply sp^2 closed concentric graphitic shells.[15] The graphitization of UDD is considered as a multistep process consisting of a decomposition of surface groups on the surface of the diamond, reconstruction of the diamond surface, initial formation of a graphitic species (*via* the transformation of the edges of diamond (111) planes into graphite (0001) planes), and their further transformation into carbon nanostructures.[16,17] Among these steps, annealed UDD (ADD) below 1200 °C is regard as an interesting sp^2/sp^3 hybrid material because it benefits from the remarkable surface properties of graphene-based nanomaterials combined with the intrinsic properties of a diamond core.[18] This promising hybrid material has high curvature and surface energy and thus exhibits more active surface physicochemical properties than other carbon materials and allows more complicated surface functionalizations.[19−22] In some cases, the modifications of UDD and ADD using functional groups involve various organic solvents and highly toxic/environmentally unfriendly reagents (*e.g.*, fluorine gas, chlorine gas) and require a prolonged reaction time with the aim to improve the particle solubility,

* Address correspondence to dssu@imr.ac.cn.

Received for review March 5, 2014 and accepted July 18, 2014.

Published online July 18, 2014
10.1021/nn501286v

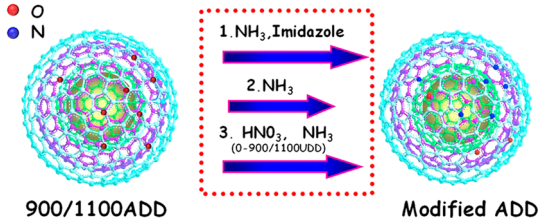

Scheme 1. Schematic illustration of the fabrication of modified ADD samples (three graphitic shells as an ideal model represent the rather irregular sp^2 carbon shells of ADD).

fluorescence, and deaggregation properties.[23−27] Therefore, exploring an alternative approach for the fabrication of modified ADD with tunable properties and applications in the catalytic reactions is very meaningful.

The selective oxidation of alcohols to their corresponding aldehydes is considered as an important organic catalytic reaction and widely applicable to the synthesis of various chemicals. Current studies on this selective oxidation reaction mainly focus on metal-related catalysts.[28] Over the past few years, carbon material catalysts have been proven to be attractive alternatives to the conventional metal or metal-based catalysts.[29] Activated carbon, graphite, carbon nanotubes (CNTs), and UDD can efficiently catalyze the dehydrogenation reactions for ethylbenzene or *n*-butane and the decomposition of methane.[30−36] The introduction of heteroatoms into nanocarbon materials is generally considered as an easy way to induce electron modulation with desired electronic structures for many catalytic processes, such as the oxygen reduction reaction (ORR) and the ring-opening polymerization.[37−40]

Starting from this point, we first study the surface nitrogen modification of ADD *via* three different methods, as it is shown in Scheme 1. The ADD samples (annealed at 900 and 1100 °C, respectively) with multiply curved graphitic shells are used as a starting material. We focus on the formation and dynamic behaviors of nitrogen species and the catalytic activity correlated to the different types of nitrogen species. The oxidation of benzylic alcohols is used to evaluate the catalytic performance over the pristine ADD and modified ADD catalysts with *tert*-butyl hydroperoxide (TBHP) as oxidant.

RESULTS AND DISCUSSION

High-resolution transmission electron microscopy (HRTEM) images in Figure 1A,B show the surfaces of 900ADD and 1100ADD samples consisting of two to four sp^2 graphitic shells. The identified interlayer spacing of 0.338 nm in the outer shell and lattice spacing of 0.204 nm in the core correspond to the (002) of graphite and (111) of diamond lattice distance, respectively. Selected area electron diffraction (SAED) patterns (inset in Figure 1A−E) composed of a few rings can be assigned to (111), (220), and (331) of the diamond structure. In addition, the prominent region in the center of the SAED pattern signifies the existence of a graphitic phase in the samples.[41] There is no obvious difference in the size of particles among the pristine and modified samples, as displayed in Figure 1C−E. The average particle size is about 5 nm. Compared with the pristine 1100ADD, modified 1100ADD samples exhibit more sp^2 graphitic shells, especially in N-1100ADD-1 and N-1100ADD-2 (Figure 1, red arrows). It could be attributed to the formation of a large number of pyridine-like defects with lone-pair electrons which requires the rearrangement of the neighboring carbon atoms.[42] The N_2 adsorption−desorption analysis indicates that there is no noticeable change of the specific surface area and the pore size of pristine ADD and modified ADD (see Table S1 and Figure S1, Supporting Information).

The content of nitrogen and oxygen in various samples was studied *via* the elemental analysis (EA) test. Figure 2 shows that the concentration of nitrogen significantly increases from 1.7 wt % for 900ADD to the highest value of 5 wt % for modified 900ADD samples, while the content of oxygen decreases from 5.2 wt % to the lowest value of 1.7 wt %. The same tendency is also observed on 1100ADD and modified 1100ADD samples. Besides, we oxidize 900ADD and 1100ADD by the liquid phase acid treatment to form the oxygen-enriched O-900 and O-1100ADD intermediate products, and then these products are used as starting materials to prepare the N-900ADD-O-2 and N-1100ADD-O-2 under ammonia gas atmosphere. As displayed in Figure 2, the introduction of nitrogen leads to a drop of oxygen content from 7.0 and 8.6 wt % of O-900 and O-1100ADD to 1.7 and 2.4 wt % of N-900ADD-O-2 and N-1100ADD-O-2, respectively. On the contrary, the nitrogen content increases from 2.8 and 2.7 wt % of N-900ADD-2 and N-1100ADD-2 (*via* direct ammonia treatment without liquid phase oxidation treatment) to 5.0 and 4.4 wt % of N-900ADD-O-2 and N-1100ADD-O-2. These results may indicate that the oxygen content plays an important role in the introduction of nitrogen. From the results of thermogravimetric analysis (TGA) (Figure 2 and Figure S2), a certain amount of mass loss of pristine 900ADD and 1100ADD samples can be attributed to the surface-adsorbed water as well as the slight decomposition of surface oxygen functional groups under elevated temperature conditions. Comparing the total content of oxygen and nitrogen by EA with the mass loss by TGA, we find that the introduced nitrogen species have not completely decomposed at 950 °C.

As displayed in Figure 3A, the spectrum of O 1s can be divided into the following regions: O1 (530.7 eV) is assigned to quinones or pyrone; O2 (531.8 eV) is attributed to a carbonyl group (C═O); O3 (532.7 eV) is a carbon−oxygen ether-like single bond. The O4 should be assigned to oxygen in pyridine-*N*-oxide and surface trace OH (can be ascribed to the sample's exposure to

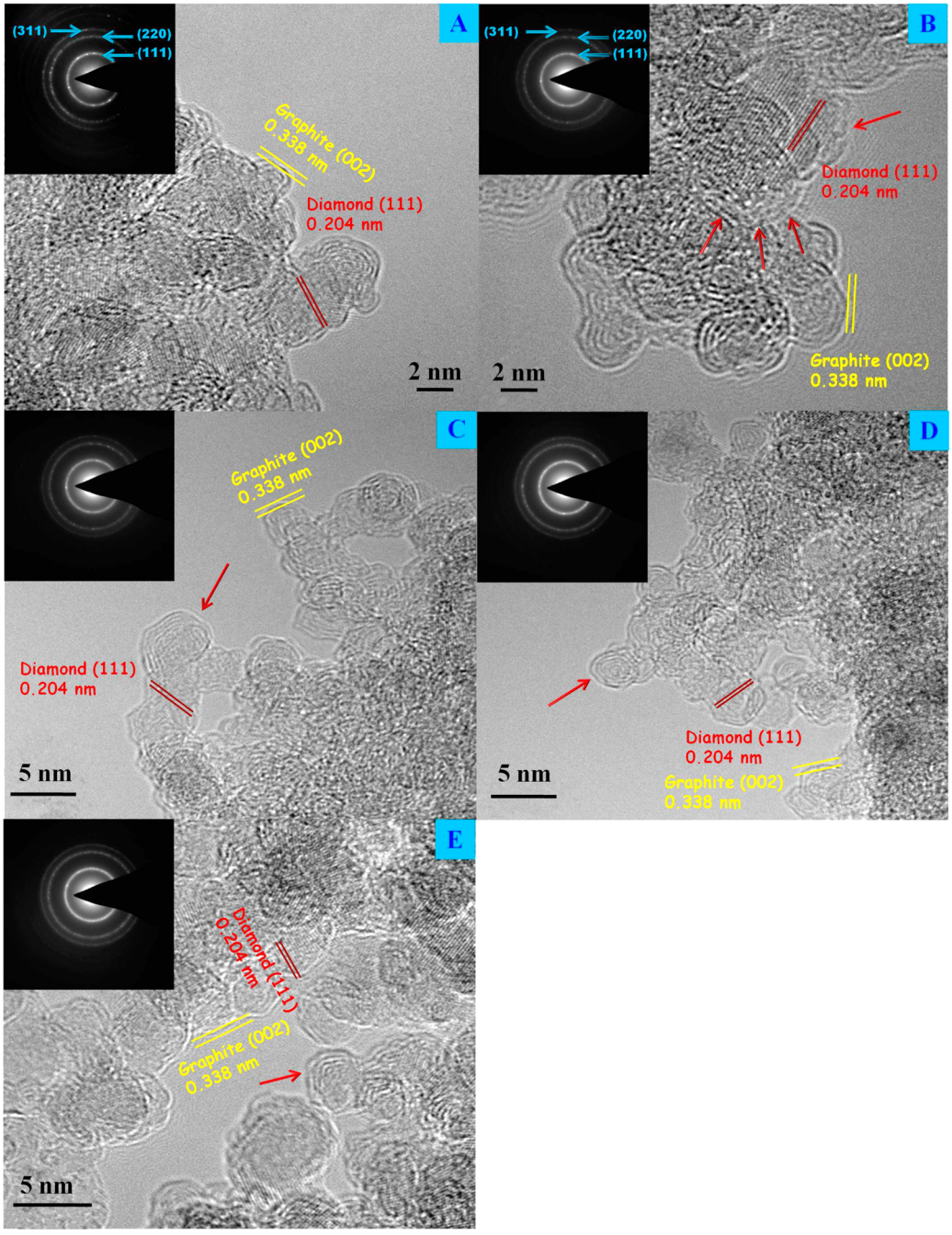

Figure 1. HRTEM images and SAED patterns (insets) of various ADD samples. (A) 900ADD, (B) 1100ADD, (C) N-1100ADD-1, (D) N-1100ADD-2, and (E) N-1100ADD-O-2. The lattice plane spacing of diamond and interlayer spacing of graphite are indicated. The SAED patterns show the typical diamond structure diffuse rings in all the samples. The red arrows indicate the graphitic shells.

atmosphere after annealing).[43−47] The N 1s spectrum (see Figure 3B) can be deconvoluted into the following five peaks: N1 (398.2 eV), N2 (399.2 eV), N3 (400.2 eV), N4 (401.3 eV), and N5 (402−405 eV), which are assigned to pyridinic nitrogen, lactam or cyano nitrogen, pyrrolic nitrogen, graphitic nitrogen, and pyridine-*N*-oxide, respectively.[48−50] In our studies, the nitrogen content can be tuned by virtue of different preparation methods. As can be seen from Figure 3B, the XPS results illustrate that the nitrogen content increases from the 1.4 at % for 900ADD (inherent) to the highest 5.4 at % for N-900ADD-1. On the contrary, the concentration of oxygen decreases from 3.7 at % to around 2.5 at % for the modified 900ADD (see Figure 3A). Moreover, a similar change tendency is found on the 1100ADD and modified 1100ADD samples (see Figure S3). The results of XPS are summarized in Figure 3C,D. The atomic ratios of O2, O3, and O4 species of all the samples decrease when nitrogen is introduced, while the O1 species nearly remains unchanged. The nitrogen

species have a significant increase compared to the pristine ADD, especially N1, N2, and N3 species. These results indicate that the nitrogen sources may react with some oxygen species by a series of chemical reactions to produce nitrogen species during the preparation process, such as nucleophilic addition. By comparing the concentration of nitrogen and oxygen of the same sample in the bulk (EA in Figure 2) and surface region (XPS in Figure 3), we find that there is an obvious difference in the nitrogen content of N-900ADD-O-2 and N-1100ADD-O-2 samples. The corresponding nitrogen content is 5.0 and 4.4 wt % by EA and 2.2 and 2.8 at % by XPS. This may be attributed to the influence of liquid phase oxidation pretreatment on the structure of the original materials (O-900ADD and O-1100ADD) of N-900ADD-O-2 and N-1100ADD-O-2.

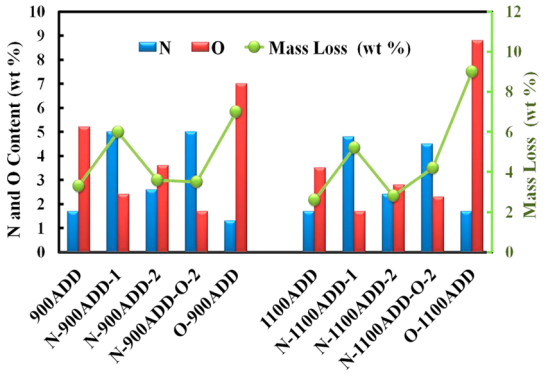

Figure 2. Comparison chart of EA (histogram) and TGA (linear graphs) in argon at a heating rate of 10 K min^{-1} over the different samples.

The surface functional groups were evidenced by diffuse reflectance FT-IR (DRIFT). As shown in Figure 4A,B, the main characteristic absorption bands of 900ADD and 1100ADD samples at 2885−2950, 1695−1725, 1550−1580, and 1315−1330 cm^{-1}/1115−1120 cm^{-1} represent C−H, C═O, C═C, and C−O vibration (phenol, ether, or similar oxygen groups).[18,51,52] The weak N−H stretching band at 3315 cm^{-1} can be found in the unmodified and modified samples. Moreover, compared with unmodified samples, the oxygen-containing bands (1695−1725, 1315−1330, and 1115−1120 cm^{-1}) on the modified samples are weakened, which are in accordance with XPS results. It should be noted that there are two new characteristic bands present on the modified samples. The absorption bands at the 2100−2200 and 1235−1245 cm^{-1} regions correspond to the C≡N and C−N stretching vibration, respectively.[52,53] The N-900ADD-O-2 and N-1100ADD-O-2 samples exhibit the most intense C≡N peak at 2100−2200 cm^{-1}, but the strongest band of C−N stretching vibration is assigned to N-900ADD-2 and N-1100ADD-2. Misra and co-workers earlier proposed that C−N stretching vibration was related to the intercalated nitrogen atoms in the sp^2 carbon network.[54]

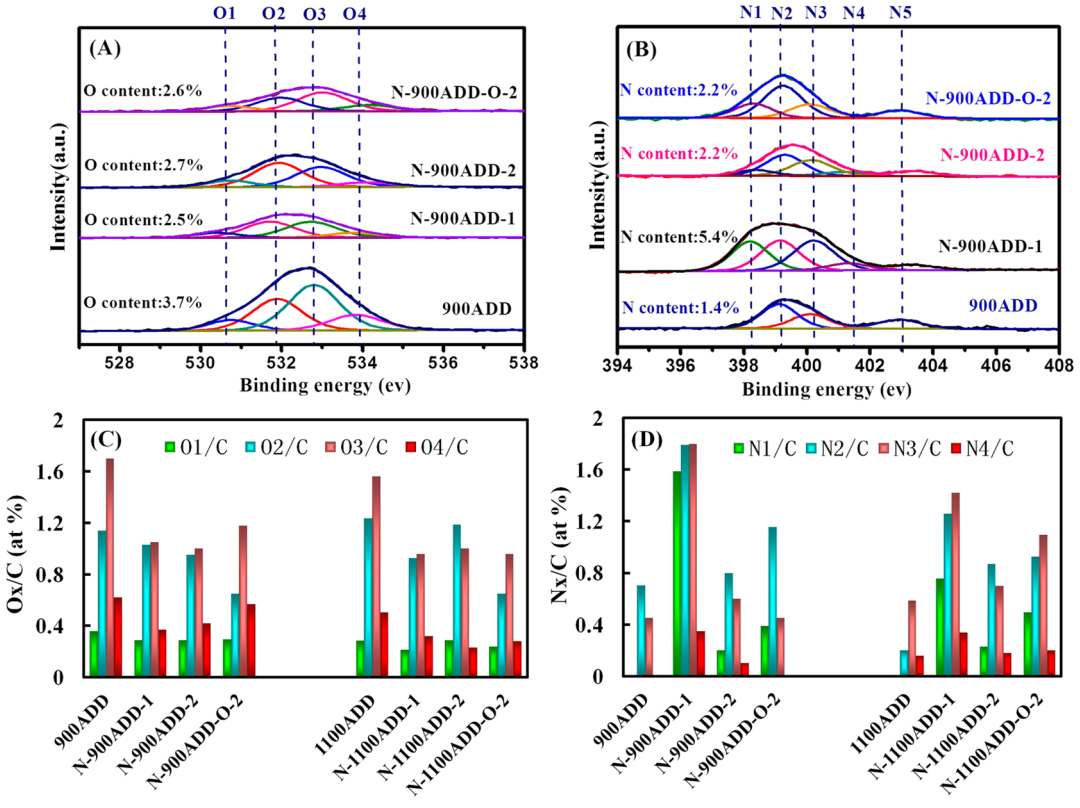

Figure 3. (A) XPS O 1s and (B) N 1s spectra of the 900ADD and modified 900ADD; (C) O_x/C and (D) N_x/C distribution diagram over the ADD and modified ADD. The XPS spectra are divided by fitting the peak maximum within ±0.2 eV and applying a full width at half-maximum (fwhm) of 1.4−1.6 eV. The value of the mixed Gaussian−Lorentzian is maintained at 40%.

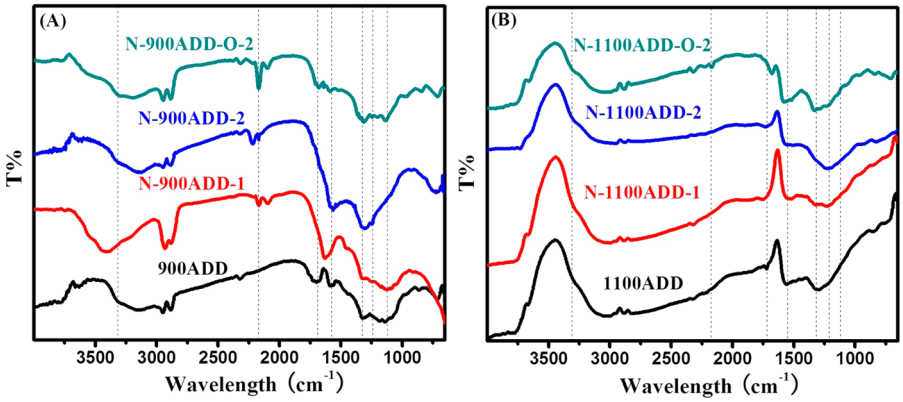

Figure 4. DRIFT spectra of various samples.

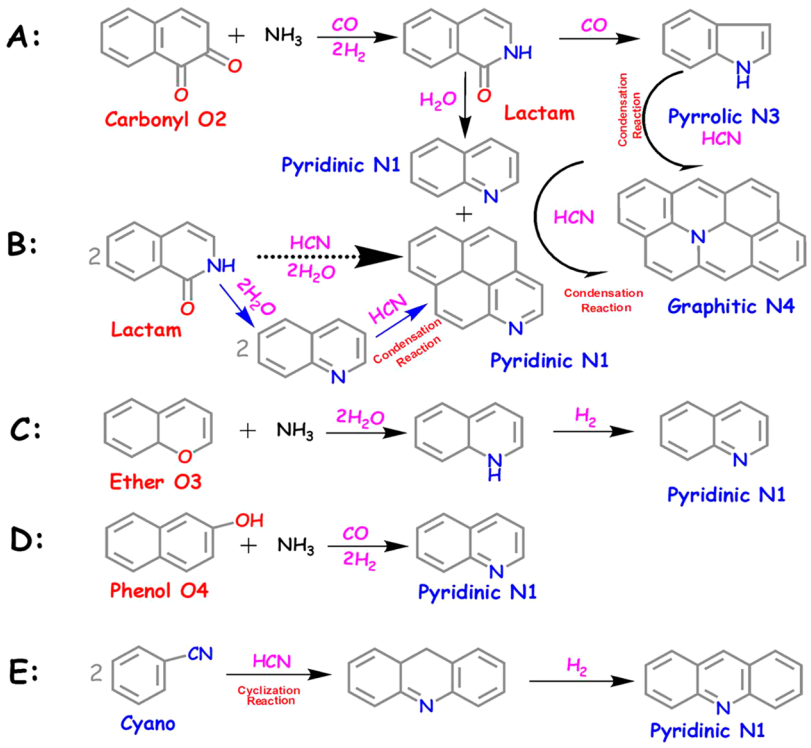

Figure 5. Schematic illustration for the formation and transformation pathways of nitrogen species (two hexatomic rings as ideal starting model structure in pathway A−D).

However, it is difficult to distinguish the assignment of the C−N bond in various nitrogen-containing groups (pyridinc, lactam, or pyrrolic) using DRIFT spectra. Due to the overlap of the C═C peak and C═N peak, the C═N absorption bands are not found in the modified samples.

After the curved graphitic shells have formed on the ADD sample (see Figure 1A,B), NH_3 and imidazole are introduced as two different nitrogen sources to achieve a modification process. Our results revealed that there is a specific relationship between oxygen species and nitrogen species. By correlating XPS data with recently reported work about other carbon materials,[55] some possible formation and transformation mechanisms of nitrogen species on the modified ADD are proposed in Figure 5. The introduction of imidazole could enhance the chemical interaction between NH_3 and the ADD surface and is favorable for forming the nitrogen species with the higher content. NH_3, a classical nucleophilic reagent, reacts with unsaturated carbonyl group O2, forming the intermediate lactam species, and releasing simultaneously CO and H_2. On the one hand, lactam species may transform directly into pyridinic N1 and pyrrole N2 species with the formation of H_2O and CO (see Figure 5A).[56] On the other hand, a couple of pyridinic N1 species originated from the dehydration of lactam species will further condense into a kind of tetracene derivative and release HCN under calcination conditions (see Figure 5B). Subsequently, a small portion of graphitic N4 species

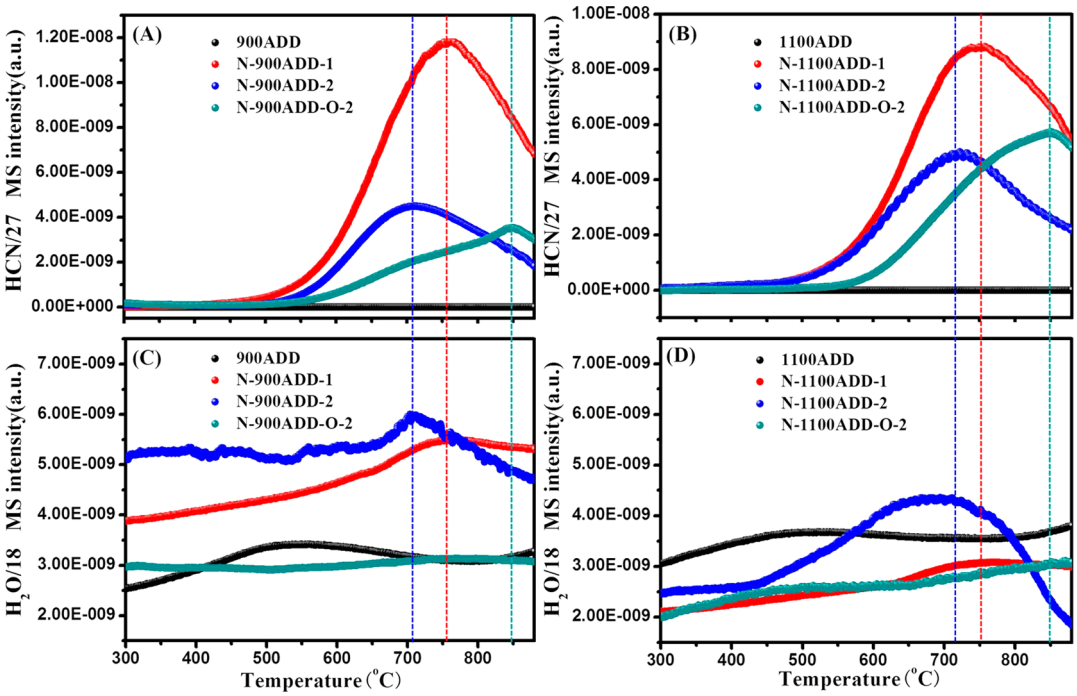

Figure 6. TPD profiles of ADD and modified ADD in helium at a heating rate of 10 K·min^{-1}, (A,B) HCN, *m/z* = 27; (C,D) H_2O, *m/z* = 18.

may be generated by the restructuration of pyridinic N1 species or pyrrolic N2 species, along with the release of HCN at high temperature. In the previous studies, Stańczyk and co-workers reported that the pyrrole nitrogen species could transform into graphitic N4 species using model chars poly(vinylpyrrolidone) as a research object upon heat treatment.[57] Wågberg and co-workers proposed that there are two transformation routes from pyridinic N1 species to graphitic N4 species.[58] As shown in Figure 5C, the ether-like O3 species can readily react with NH_3 *via* the dehydration process, accompanying the appearance of water. Further dehydration leads to the formation of pyridinic N1 species and the release of H_2.[59] The trace phenol O4 will generate pyridinic N1, CO, and H_2 by reacting with NH_3 (see Figure 5D).[55] Moreover, cyano species stemmed from chemical combination between nitrogen sources and surface defects or surface oxygen groups will cyclize though a self-polymerization process, and then, conjugated imines are formed. With further heat treatment, hydrogen may be released and a series of pyridine N1 species can be obtained (see Figure 5E). Similar results have been proven in the pyrolysis evolution of cyano species over the model chars polyacrylonitrile (PAN).[48] All these possible pathways illustrate the surface reconstruction of the modified samples.

On the basis of the above results, we proposed that the formation pathways of HCN involved the transformation of lactam and cyano species as well as the decomposition and rearrangement of pyridinic N1 or pyrrolic N3 species. To further study the transformation behaviors of nitrogen-containing species, temperature-programmed desorption (TPD) was performed. Figure 6A,B show that the HCN signal starts to increase when the temperature is greater than 500 °C, indicating that those of nitrogen-containing species start to transform into pyridinic N1 species.[60] Increasing the temperature, the HCN signal evaluation of N-900ADD-2 and N-1100ADD-2 attains a maximum value and the corresponding H_2O peak located at 710 °C is also observed (see Figure 6C,D). Moreover, we find that the HCN and H_2O signals of N-900ADD-1 and N-1100ADD-1 retard and shift to 760 °C due to the higher nitrogen content. These phenomena indicate that the HCN at these temperature regions mainly derives from the transformation of lactam into pyridinic N1 species. Interestingly, the strongest HCN signal peak of N-900ADD-O-2 and N-1100ADD-O-2 can be found at 850 °C, while the sharp peak of H_2O is not obtained. It reveals that the HCN above 760 °C originates from the decomposition and restructuration of pyridinic N1, pyrrolic N3, and cyclization of cyano species. Compared with other kinds of modified samples, cyano species rather than lactam may account for a major proportion in N2 species of N-900ADD-O-2 and N-1100ADD-O-2. This assumption is confirmed by DRIFT analysis. The broad H_2O signal evaluations of the 900ADD and 1100ADD at 550 °C are assigned to the release of trace phenol O4 species as displayed in Figure 6C,D. The TPD results well support the proposed pathways for the transformation of nitrogen species at high temperature.

The selective oxidation of benzylic alcohols was used as a probe for catalytic performance. As can be seen in Figure 7A,B, the conversion of benzyl alcohol on the modified 900ADD catalysts is between 10.5 and

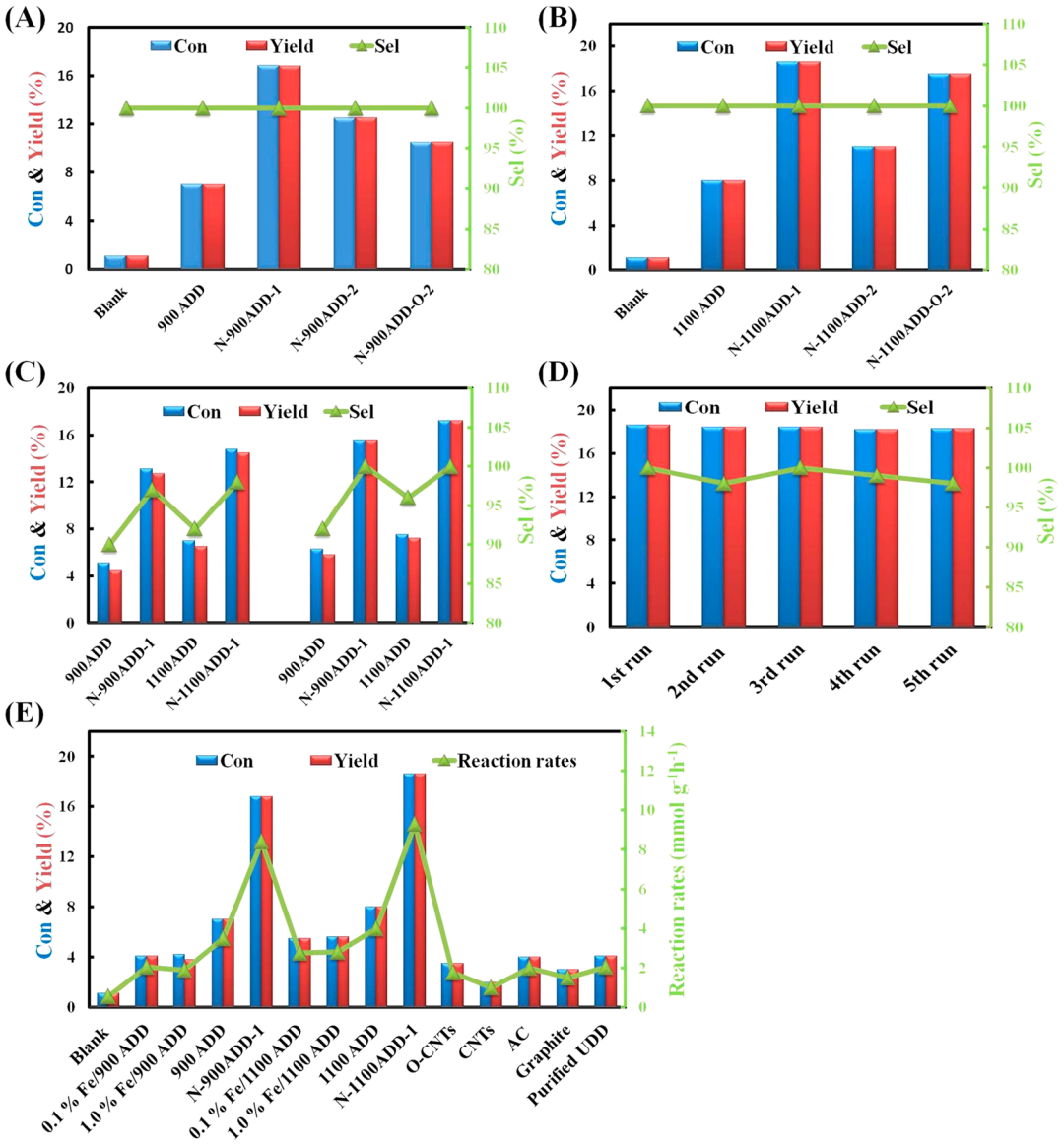

Figure 7. (A,B) Catalytic performance of various samples in the selective oxidation of benzyl alcohol to benzaldehyde. (C) Catalytic performance of different samples in the selective oxidation of 4-methylbenzyl alcohol to 4-methylbenzaldehyde (the left side of figure) and 4-nitrobenzyl alcohol to 4-nitrobenzaldehyde (the right side of figure). (D) Stability tests of N-1100ADD-1 in the selective oxidation of benzyl alcohol to benzaldehyde. (E) Catalytic performance and reaction rates of various reference samples in the selective oxidation of benzyl alcohol to benzaldehyde; $Fe(NO_3)_3$ as precursor, impregnated for 24 h and dried at 353 K. Catalytic reaction conditions: 2 mmol substrates, 0.01 g of catalyst, 2 mmol TBHP, 343 K, 4 h. Internal standard: ethylbenzene. The reaction rate = yield (%) × substrate molar (mmol)/[reaction time (h) × catalyst mass (g)].

16.8%, while a conversion of 7% is obtained on pristine 900ADD catalyst. The highest conversion of benzyl alcohol on the modified 1100ADD catalysts reaches 18.6%, 2-fold higher than that of pristine 1100ADD catalyst. All nitrogen-modified catalysts exhibit a significant improvement in the selective oxidation of benzyl alcohol to benzaldehyde. It should be noted that when the other two kinds of substrates (4-methylbenzyl alcohol and 4-nitrobenzaldehyde) are used to evaluate the catalytic performance, the modified catalysts also exhibit more excellent catalytic performance than those of unmodified catalysts (Figure 7C). Among all the catalysts, N-1100ADD-1 with the best catalytic performance is selected for cycle tests. As displayed in Figure 7D, the catalyst exhibits good activity stability toward the selective oxidation of benzyl alcohol for the tested five successive runs. Moreover, Fe-containing 900ADD and 1100ADD catalysts with different contents (0.1 and 1.0%) cannot improve the catalytic performance in the selective oxidation of benzyl alcohol. The reaction rates decrease from 8.4 and 9.3 mmol/g·h for the N-900ADD-1 and N-1100ADD-1 to about 2.0 and 2.8 mmol/g·h for Fe-containing 900ADD and 1100ADD. Additionally, the modified catalysts also exhibit higher reaction rates than other carbon materials (Figure 7E).

In order to understand the nature of modified catalysts for the selective oxidation of benzylic alcohols, the correlation between nitrogen content and the

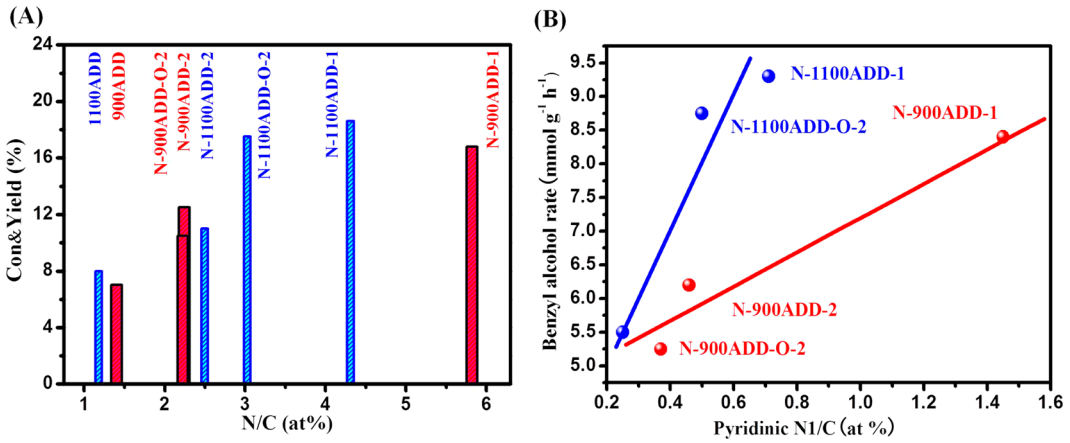

Figure 8. (A) Diagram of total content of nitrogen and catalytic performance of various samples toward the selective oxidation of benzyl alcohol. (B) Relationship between benzyl alcohol conversion rate and pyridinic N1/C atomic ratio of modified ADD.

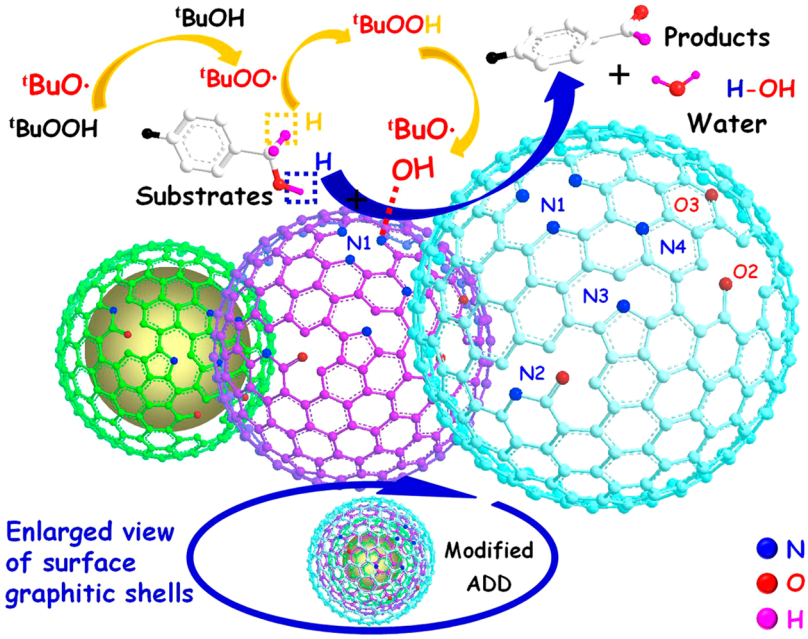

Scheme 2. Mechanism diagram of catalytic reaction for benzylic alcohols on the modified ADD (three graphitic shells are used as an ideal catalyst model).

catalytic activity was studied. As shown in Figure 8A, all the modified ADD catalysts show a significant improvement in the catalytic performance. The active sites of carbon materials in the gas phase reactions, such as oxidative dehydrogenation, dehydration of alcohols, and NOx reduction, are attributed to the quinones, carboxylic acids, carboxyl, and lactones.[31,61−63] Introducing the nitrogen into carbon materials alters the surface physicochemical properties (*e.g.*, surface electron density, alkalinity or acidity, and defects) and thus nitrogen species play a decisive role in a series of catalytic reactions, such as the hydrogen peroxide synthesis, catalytic ozonation, H_2S oxidation, and wet air oxidation.[64−67] Ma *et al.* reported that the graphitic nitrogen plays a key role in enhancing catalytic performance by changing the electronic structure of the adjacent carbon atoms.[68]

We plot the nitrogen species/C atomic ratio *versus* the reaction rate, as shown in Figure 8B. A linear relationship is found between the pyridinic N1/C atomic ratio and the benzyl alcohol conversion rate. There is no correlation between the catalytic activity with other kinds of species, including N2, N4 and O1, O2, O3 species (Figure S4). A synergistic effect between the carbonyl O2 species and nitrogen species is not observed (based on O2 + N1). It seems that the pyridinic N1 is closely correlated with the benzyl alcohol catalytic oxidation. Interestingly, N-900ADD-O-2 and N-1100ADD-O-2 with very similar atomic ratios of pyridinic N1/C exhibit a different catalytic performance, which can be attributed to the different degree of graphitization. It is suggested in literature that a lone pair of electrons in pyridinic N1 endows the materials a more active physicochemical

property.[65] Recently, pyridinic N1 has also been reported to be the most active sites for catalyzing in ORR, sulfur dioxide removal, and dehydrohalogenation due to the formation of chemically active sites (*e.g.*, pyridine-like defects), localized areas of higher electron density in the catalytic reaction.[69] Thus, it is not simply the nitrogen content but the nitrogen-bonding configurations that could be the key factor to implement the catalytic activity of modified carbon materials. So, it is reasonable to believe that the pyridinic N1 is accountable for the selective oxidation of benzylic alcohols.

Based on free radical theory and the special property of the pyridinic N1,[70] a possible reaction pathway is proposed. Pyridinic N1 as a hydrogen bond acceptor reacts with the •OH free radical, which is derived from the decomposition of ^{t}BuOOH, forming pyridinic N1−OH active species.[71] Such active species will capture a hydrogen atom on the alcoholic hydroxyl group of the $-CH_2OH$, giving rise to the release of water and the formation of a $-CH_2O$ group. The intermediate free radical ^{t}BuOO• that originated from the reaction of the decomposer ^{t}BuO• with a portion of ^{t}BuOOH can activate the C−H bond of the $-CH_2O$ group,[72,73] finally leading to the formation of a −CHO group and ^{t}BuOOH under mild conditions. The detailed catalytic mechanism process is displayed in Scheme 2.

CONCLUSIONS

In summary, we have developed a new class of nitrogen-modified ADD samples (900ADD and 1100ADD with multilayers graphitic shells as starting materials) *via* three different preparation approaches. Surface oxygen groups have been demonstrated to play a key role in the nitrogen-modified process, and lactam and cyano species are important intermediates in the formation of various nitrogen species. Among all the modified 900ADD and 1100ADD samples, the highest content of nitrogen reaches 5.3 and 4.0 at %, respectively. Such nitrogen-rich phenomenon can provide a higher density of catalytic active centers (pyridinic N1), evidenced by the efficient oxidation of benzylic alcohols to benzylic aldehydes in the presence of TBHP. The detailed mechanism of the catalytic reaction is mainly based on the bonding behavior between the pyridinic N1 species with lone electron property and the free radicals. Our work opens a new aspect for the further study of the modified graphite-related materials in all fields (*e.g.*, C−H activation and ORR).

METHODS

Materials. Purified ultradispersed nanodiamond was purchased from Beijing Grish Hitech Co. (China), produced by detonation and followed by acid washing. The noncombustible contaminations were tested by an inductively coupled plasma emission spectrometer and included Fe < 50 ppm, Cr < 10 ppm, Al < 50 ppm, Cu < 10 ppm, Mg < 10 ppm, Ti < 10 ppm, and Ca < 50 ppm. The average particle size was about 5 nm. Benzyl alcohol, benzaldehyde, ethylbenzene, trifluorotoluene and *tert*-butyl hydroperoxide and activated carbon were supplied by Alfa reagent. Graphite and carbon nanotubes were provided by ACHESON Co. Ltd. and Tsinghua University, respectively. All chemicals were analytical grade without further purification.

Sample Preparation. The fabrication of samples was proceeded by a two-step process: (1) 900ADD and 1100ADD with graphitic shell structures were produced by annealing purified UDD at 900 and 1100 °C for 4 h in argon atmosphere, respectively. (2) Three different preparation methods were applied to synthesize the modified ADD samples. Method 1: 0.2 g of as-prepared 900 or 1100ADD sample was evenly spread in the tube furnace and calcined at 550 °C (at a heating rate of 5 °C/min) for 2 h under ammonia gas (150 mL/min). Then, the imidazole vapor (*via* 5 g imidazole powder heated from 50 to 250 °C within 30 min in one end of the furnace) was further transported into the other end of tube furnace by virtue of ammonia gas and maintained at 550 °C. After calcination for 2.5 h, the furnace was cooled naturally to room temperature. The final products were labeled as N-900ADD-1 and N-1100ADD-1. Method 2a: 0.2 g of as-prepared 900 or 1100ADD was directly calcined at 550 °C for 4 h under ammonia gas. The final products were designated as N-900ADD-2 and N-1100ADD-2. Method 2b: 0.5 g of as-prepared 900 or 1100ADD sample was added to 100 mL of concentrated nitric acid with continuous stirring at 120 °C for 2 h. The products were filtered and washed with deionized water and ethanol and then dried at 60 °C for several hours. The products were denoted as O-900ADD and O-1100ADD. The O-900 and O-1100ADD were further calcined at 550 °C for 4 h under ammonia gas. The final samples were labeled as N-900ADD-3 and N-1100ADD-3. In addition, O-CNTs were obtained by the oxidation of CNTs in concentrated nitric acid to continuous stirring at 120 °C for 4 h and subsequently filtered, washed, and dried at 60 °C.

Characterization. Elemental analysis was recorded on LECO TCH-600, an analyzer dedicated to quantitatively test N, H, and O elements *via* the detection of corresponding products N_2, H_2, and CO_2. High-resolution transmission electron microscopy images were achieved on a FEI Tecnai G2 F20 microscope. Temperature-programmed desorption was performed on a tube furnace and an AVI Omnistar mass spectrometer. The atmosphere was He, and the heating rate was 10 °C/min from 50 to 900 °C. Thermogravimetric analysis and differential scanning calorimetry were recorded on a Netzsch-STA 449 F3 instrument. The atmosphere was N_2, and the heating rate was 10 °C/min from 35 to 950 °C. Diffuse reflectance FT-IR spectra were collected at a resolution of 4 cm^{-1} on Nicolet iZ10. The X-ray photoelectron spectroscopy (XPS) spectra were carried out on an ESCALAB 250 XPS system with a monochromatized Al Kα X-ray source. The XPS spectra were divided by fitting the peak maximum within ±0.2 eV and applying a fwhm of 1.4−1.6 eV by means of Avantage analysis soft. The value of the mixed Gaussian−Lorentzian was maintained at 40%.

Catalytic Activity Testing. The oxidation reactions were carried out in a two-necked flask containing 0.01 g of catalyst, 10 mL of trifluorotoluene, 2 mmol benzyl alcohol, and 2 mmol TBHP (65 wt %) at 70 °C for 4 h. TBHP is a common oxidant in the catalytic reactions because it is easy to generate various intermediate radicals (*e.g.*, •OH, ^{t}BuO•, ^{t}BuOO•, and •H). Depending on the different reactions,[71−75] the reaction mechanism pathways of those radicals may concisely include the following: (1) The radicals can activate the substrates and further form the excited state substrates under mild condition. Subsequently, the latter will be catalyzed by the active sites of catalysts, and the desired products are finally obtained. (2) The radicals may directly react with the active sites of catalysts to form an active site−radical complex. This complex is able to activate the substrates and gain the desired products. A certain amount of ethylbenzene as an internal standard was added to the solution.

The reaction solution was sampled periodically and analyzed using gas chromatography (Agilent 7890A).

Conflict of Interest: The authors declare no competing financial interest.

Acknowledgment. The authors thank Dr. Linhui Yu, Bingsen Zhang, Honyang Liu, Xiaoli Pan, Rui Huang, Shanjun Mao, and Xianmo Gu for their kind help on this study. The authors acknowledge the financial support from MOST (2011CBA00504), NSFC of China (21133010, 51221264, 21261160487), and "Strategic Priority Research Program" of the Chinese Academy of Sciences, Grant No. XDA09030103.

Supporting Information Available: Materials of additional dates and figures for XPS spectra, BET analysis for various 900ADD and 1100ADD samples, relationship between benzyl alcohol conversion rate and other kinds of nitrogen or oxygen species' atomic ratios of modified ADD. This material is available free of charge *via* the Internet at http://pubs.acs.org.

REFERENCES AND NOTES

1. Su, D. S.; Perathoner, S.; Centi, G. Nanocarbons for the Development of Advanced Catalysts. *Chem. Rev.* **2013**, *113*, 5782–5816.
2. Su, D. S.; Schlögl, R. Nanostructured Carbon and Carbon Nanocomposites for Electrochemical Energy Storage Applications. *ChemSusChem* **2010**, *3*, 136–168.
3. Vilatela, J. J.; Eder, D. Nanocarbon Composites and Hybrids in Sustainability: A Review. *ChemSusChem* **2012**, *5*, 456–478.
4. Roth, S.; Park, H. J. Nanocarbonic Transparent Conductive Films. *Chem. Soc. Rev.* **2010**, *39*, 2477–2483.
5. D'Souza, F.; Ito, O. Photosensitized Electron Transfer Processes of Nanocarbons Applicable to Solar Cells. *Chem. Soc. Rev.* **2012**, *41*, 86–96.
6. Sun, X. Y.; Wang, R.; Su, D. S. Research Progress in Metal-Free Carbon-Based Catalysts. *Chin. J. Catal.* **2013**, *34*, 508–523.
7. Wang, D. W.; Su, D. S. Heterogeneous Nanocarbon Materials for Oxygen Reduction Reaction. *Energy Environ. Sci.* **2014**, *7*, 576–591.
8. Chen, M.; Zhang, X. Q.; Man, H. B.; Lam, R.; Chow, E. K.; Ho, D. Nanodiamond Vectors Functionalized with Polyethylenimine for SiRNA Delivery. *J. Phys. Chem. Lett.* **2010**, *1*, 3167–3171.
9. Yuan, Y.; Wang, X.; Jia, G.; Liu, J. H.; Wang, T.; Gu, Y.; Yang, S. T.; Zhen, S.; Wang, H.; Liu, Y. Pulmonary Toxicity and Translocation of Nanodiamonds in Mice. *Diamond Relat. Mater.* **2010**, *19*, 291–299.
10. Yuan, J.; Li, H.; Gao, S.; Lin, Y.; Li, H. A Facile Route to n-Type TiO_2-Nanotube/p-Type Boron-Doped-Diamond Heterojunction for Highly Efficient Photocatalysts. *Chem. Commun.* **2010**, *46*, 3119–3121.
11. Tisler, J.; Reuter, R.; Lämmle, A.; Jelezko, F.; Balasubramanian, G.; Hemmer, P. R.; Reinhard, F.; Wrachtrup, J. Highly Efficient FRET from a Single Nitrogen-Vacancy Center in Nanodiamonds to a Single Organic Molecule. *ACS Nano* **2011**, *5*, 7893–7898.
12. Matsumoto, N.; Joly, P. L.; Kinoshita, H.; Ohmae, N. Application of Onion-like Carbon to Micro and Nanotribology. *Diamond Relat. Mater.* **2007**, *16*, 1227–1230.
13. Sankaran, K. J.; Kumar, N.; Kurian, J.; Ramadoss, R.; Chen, H. C.; Dash, S.; Tyagi, A. K.; Lee, C. Y.; Tai, N. H.; Lin, I. N. Improvement in Tribological Properties by Modification of Grain Boundary and Microstructure of Ultrananocrystalline Diamond Films. *ACS Appl. Mater. Interfaces* **2013**, *5*, 3614–3624.
14. Raty, J. Y.; Galli, A. G. Ultradispersity of Diamond at the Nanoscale. *Nat. Mater.* **2003**, *2*, 792–795.
15. Panich, A. M.; Shames, A. I.; Sergeev, N. A.; Olszewski, M.; McDonough, J. K.; Mochalin, V. N.; Gogotsi, Y. Nanodiamond Graphitization: A Magnetic Resonance Study. *J. Phys.: Condens. Matter* **2013**, *25*, 245303.
16. Kuznetsov, V. L.; Butenko, Y. V. Diamond Phase Transitions at Nanoscale. *Ultananocrystalline Diamond*, 2nd ed.; Shenderova, O. A., Gruen, D. M., Eds.; William Andrew Publishing: Oxford, 2012; Chapter 7, pp 181−244.
17. Kuznetsov, V. L.; Chuvilin, A. L.; Butenko, Y. V.; Stankus, S. V.; Khairulin, R. A.; Gutakovskii, A. K. Closed Curved Graphite-like Structures Formation on Micron-Size Diamond. *Chem. Phys. Lett.* **1998**, *289*, 353–360.
18. Petit, T.; Arnault, J. C.; Girard, H. A.; Sennour, M.; Kang, T. Y.; Cheng, C. L.; Bergonzo, P. Oxygen Hole Doping of Nanodiamond. *Nanoscale* **2012**, *4*, 6792–6799.
19. Mochalin, V. N.; Shenderova, O.; Ho, D.; Gogotsi, Y. The Properties and Applications of Nanodiamonds. *Nat. Nanotechnol.* **2012**, *7*, 11–23.
20. Krueger, A.; Lang, D. Functionality Is Key: Recent Progress in the Surface Modification of Nanodiamond. *Adv. Funct. Mater.* **2012**, *22*, 890–906.
21. Jarre, G.; Liang, Y.; Betz, P.; Lang, D.; Krueger, A. Playing the Surface Game: Diels−Alder Reactions on Diamond Nanoparticles. *Chem. Commun.* **2011**, *47*, 544–546.
22. Liang, Y.; Meinhardt, T.; Jarre, G.; Ozawa, M.; Vrdoljak, P.; Schöll, A.; Reinert, F.; Krueger, A. Deagglomeration and Surface Modification of Thermally Annealed Nanoscale Diamond. *J. Colloid Interface Sci.* **2011**, *354*, 23–30.
23. Martín, R.; Heydorn, P. C. N.; Alvaro, M.; Garcia, H. General Strategy for High-Density Covalent Functionalization of Diamond Nanoparticles Using Fenton Chemistry. *Chem. Mater.* **2009**, *21*, 4505–4514.
24. Spitsyn, B. V.; Denisov, S. A.; Skorik, N. A.; Chopurova, A. G.; Parkaeva, S. A.; Belyakova, L. D.; Larionov, O. G. The Physical−Chemical Study of Detonation Nanodiamond Application in Adsorption and Chromatography. *Diamond Relat. Mater.* **2010**, *19*, 123–127.
25. Liu, Y.; Gu, Z.; Margrave, J. L.; Khabashesku, V. N. Functionalization of Nanoscale Diamond Powder: Fluoro-, Alkyl-, Amino-, and Amino Acid-Nanodiamond Derivatives. *Chem. Mater.* **2004**, *16*, 3924–3930.
26. Park, C. L.; Jee, A. Y.; Lee, M.; Lee, S. Gelation, Functionalization, and Solution Behaviors of Nanodiamonds with Ionic Liquids. *Chem. Commun.* **2009**, 5576–5578.
27. Ray, M. A.; Tyler, T.; Hook, B.; Martin, A.; Cunningham, G.; Shenderova, O.; Davidson, J. L.; Howell, M.; Kang, W. P.; McGuire, G. Cool Plasma Functionalization of Nano-crystalline Diamond Films. *Diamond Relat. Mater.* **2007**, *16*, 2087–2089.
28. Sheldon, R. A.; Dijksman, A. Green, Catalytic Oxidations of Alcohols. *Acc. Chem. Res.* **2002**, *35*, 774–781.
29. Su, D. S.; Zhang, J.; Frank, B.; Thomas, A.; Wang, X.; Paraknowitsch, J.; Schlögl, R. Metal-Free Heterogeneous Catalysis for Sustainable Chemistry. *ChemSusChem* **2010**, *3*, 169–180.
30. Drago, R. S.; Jurczyk, K. Oxidative Dehydrogenation of Ethylbenzene to Styrene over Carbonaceous Catalysts. *Appl. Catal., A* **1994**, *112*, 117–124.
31. Pereira, M. F. R.; Órfão, J. J. M.; Figueiredo, J. L. Oxidative Dehydrogenation of Ethylbenzene on Activated Carbon Fibers. *Carbon* **2002**, *40*, 2393–2401.
32. Guerrero, R. A.; Rodríguez, R. I. Oxydehydrogenation of Ethylbenzene to Styrene Catalyzed by Graphites and Activated Carbons. *Carbon* **1994**, *32*, 23–29.
33. Zhang, J.; Liu, X.; Blume, R.; Zhang, A.; Schlögl, R.; Su, D. S. Surface-Modified Carbon Nanotubes Catalyze Oxidative Dehydrogenation of *n*-Butane. *Science* **2008**, *322*, 73–77.
34. Su, D.; Maksimova, N. I.; Mestl, G.; Kuznetsov, V. L.; Keller, V.; Schlögl, R.; Keller, N. Oxidative Dehydrogenation of Ethylbenzene to Styrene over Ultra-dispersed Diamond and Onion-like Carbon. *Carbon* **2007**, *45*, 2145–2151.
35. Zhang, J.; Su, D. S.; Blume, R.; Schlögl, R.; Wang, R.; Yang, X.; Gajović, A. Surface Chemistry and Catalytic Reactivity of a Nanodiamond in the Steam-Free Dehydrogenation of Ethylbenzene. *Angew. Chem., Int. Ed.* **2010**, *49*, 8640–8644.
36. Zhong, B. W.; Zhang, J.; Su, D. S. Insight into the Mechanism of Nanodiamond Catalysed Decomposition of Methane Molecules. *Phys. Chem. Chem. Phys.* **2014**, *16*, 4488–4491.

37. Liu, Y.; Chen, S.; Quan, X.; Yu, H.; Zhao, H.; Zhang, Y.; Chen, G. Boron and Nitrogen Codoped Nanodiamond as an Efficient Metal-Free Catalyst for Oxygen Reduction Reaction. *J. Phys. Chem. C* **2013**, *117*, 14992–14998.
38. Rao, C. V.; Cabrera, C. R.; Ishikawa, Y. In Search of the Active Site in Nitrogen-Doped Carbon Nanotube Electrodes for the Oxygen Reduction Reaction. *J. Phys. Chem. Lett.* **2010**, *1*, 2622–2627.
39. Qu, L.; Liu, Y.; Baek, J. B.; Dai, L. Nitrogen-Doped Graphene as Efficient Metal-Free Electrocatalyst for Oxygen Reduction in Fuel Cells. *ACS Nano* **2010**, *4*, 1321–1326.
40. Yu, H.; Peng, F.; Tan, J. Selective Catalysis of the Aerobic Oxidation of Cyclohexane in the Liquid Phase by Carbon Nanotubes. *Angew. Chem., Int. Ed.* **2011**, *50*, 3978–3982.
41. Sankaran, K. J.; Lin, Y. F.; Jian, W. B.; Chen, H. C.; Panda, K.; Sundaravel, B.; Dong, C. L.; Tai, N. H.; Lin, I. N. Structural and Electrical Properties of Conducting Diamond Nanowires. *ACS Appl. Mater. Interfaces* **2013**, *5*, 1294–1301.
42. Cho, Y. J.; Kim, H. S.; Baik, S. Y.; Myung, Y.; Jung, C. S.; Kim, C. H.; Park, J.; Kang, H. S. Nitrogen-Doped Graphitic Layers Deposited on Silicon Nanowires for Efficient Lithium-Ion Battery Anodes. *J. Phys. Chem. C* **2011**, *115*, 9451–9457.
43. Arrigo, R.; Hävecker, M.; Wrabetz, S.; Blume, R.; Lerch, M.; McGregor, J.; Parrott, E. P. J.; Zeitler, J. A.; Gladden, L. F.; Knop, G. A.; *et al.* Tuning the Acid/Base Properties of Nanocarbons by Functionalization *via* Amination. *J. Am. Chem. Soc.* **2010**, *132*, 9616–9630.
44. Walczyk, M.; Swiatkowski, A.; Pakula, M.; Biniak, S. Electrochemical Studies of the Interaction between a Modified Activated Carbon Surface and Heavy Metal Ions. *J. Appl. Electrochem.* **2005**, *35*, 123–130.
45. Agnès, C.; Arnault, J. C.; Omnès, F.; Jousselme, B.; Billon, M.; Bidan, G.; Mailley, P. XPS Study of Ruthenium Tris-Bipyridine Electrografted from Diazonium Salt Derivative on Microcrystalline Boron Doped Diamond. *Phys. Chem. Chem. Phys.* **2009**, *11*, 11647–11654.
46. Zeppilli, S.; Arnault, J. C.; Gesset, C.; Bergonzo, P.; Polini, R. Thermal Stability and Surface Modifications of Detonation Diamond Nanoparticles Studied with X-ray Photoelectron Spectroscopy. *Diamond Relat. Mater.* **2010**, *19*, 846–853.
47. Arnault, J. C.; Saada, S.; Nesladek, M.; Williams, O. A.; Haenen, K.; Bergonzo, P.; Osawa, E. Diamond Nanoseeding on Silicon: Stability under H2MPCVD Exposures and Early Stages of Growth. *Diamond Relat. Mater.* **2008**, *17*, 1143–1149.
48. Pels, J. R.; Kapteijn, F.; Moulijn, J. A.; Zhu, Q.; Thomas, K. M. Evolution of Nitrogen Functionalities in Carbonaceous Materials during Pyrolysis. *Carbon* **1995**, *33*, 1641–1653.
49. Kelemen, S. R.; Gorbaty, M. L.; Kwiatek, P. J. Quantification of Nitrogen Forms in Argonne Premium Coals. *Energy Fuels* **1994**, *8*, 896–906.
50. Boudou, J. P.; Chehimi, M.; Broniek, E.; Siemieniewska, T.; Bimer, J. Adsorption of H_2S or SO_2 on an Activated Carbon Cloth Modified by Ammonia Treatment. *Carbon* **2003**, *41*, 1999–2007.
51. Arnault, J. C.; Petit, T.; Girard, H.; Chavanne, A.; Gesset, C.; Sennour, M.; Chaigneau, M. Surface Chemical Modifications and Surface Reactivity of Nanodiamonds Hydrogenated by CVD Plasma. *Phys. Chem. Chem. Phys.* **2011**, *13*, 11481–11487.
52. Geng, D.; Yang, S.; Zhang, Y.; Yang, J.; Liu, J.; Li, R.; Sham, D. K.; Sun, X.; Ye, S.; Knights, S. Nitrogen Doping Effects on the Structure of Graphene. *Appl. Surf. Sci.* **2011**, *257*, 9193–9198.
53. Kaufman, J. H.; Metin, S. Symmetry Breaking in Nitrogen-Doped Amorphous Carbon: Infrared Observation of the Raman-Active G and D Bands. *Phys. Rev. B* **1989**, *39*, 13053–13060.
54. Misra, A.; Tyagi, P. K.; Singh, M. K.; Misra, D. S. FTIR Studies of Nitrogen Doped Carbon Nanotubes. *Diamond Relat. Mater.* **2006**, *15*, 385–388.
55. Kundu, S.; Xia, W.; Muhler, M. The Formation of Nitrogen-Containing Functional Groups on Carbon Nanotube Surfaces: A Quantitative XPS and TPD Study. *Phys. Chem. Chem. Phys.* **2010**, *12*, 4351–4359.
56. Jansen, R. J. J.; Bekkum, H. V. Amination and Ammoxidation of Activated Carbons. *Carbon* **1994**, *32*, 1507–1516.
57. Stańczyk, K.; Dziembaj, R.; Piwowars, Z.; Witkowski, S. Transformation of Nitrogen Structures in Carbonization of Model Compounds Determined by XPS. *Carbon* **1995**, *33*, 1383–1392.
58. Sharifi, T.; Hu, G.; Jia, X.; Wågberg, T. Formation of Active Sites for Oxygen Reduction Reactions by Transformation of Nitrogen Functionalities in Nitrogen-Doped Carbon Nanotubes. *ACS Nano* **2012**, *6*, 8904–8912.
59. Voll, M.; Bonhem, H. P. Basische Oberflächenoxide auf Kohlenstoff—IV. Chemische Reaktionen zur Identifizierung der Oberflächengruppen. *Carbon* **1971**, *9*, 481–488.
60. Arrigo, R.; Hävecker, M.; Schlögl, R.; Su, D. S. Dynamic Surface Rearrangement and Thermal Stability of Nitrogen Functional Groups on Carbon Nanotubes. *Chem. Commun.* **2008**, 4891–4893.
61. Figueiredo, J. L.; Pereira, M. F. R. The Role of Surface Chemistry in Catalysis with Carbons. *Catal. Today* **2010**, *150*, 2–7.
62. Carrasco, M. F.; Mueden, A.; Moreno, C. C. Surface-Treated Activated Carbons as Catalysts for the Dehydration and Dehydrogenation Reactions of Ethanol. *J. Phys. Chem. B* **1998**, *102*, 9239–9244.
63. Mochida, I.; Korai, Y.; Shirahama, M.; Kawano, S.; Hada, T.; Seo, Y.; Yoshikawa, M.; Yasutake, A. Removal of SOx and NOx over Activated Carbon Fibers. *Carbon* **2000**, *38*, 227–239.
64. Fellinger, T. P.; Hasché, F.; Strasser, P.; Antonietti, M. Mesoporous Nitrogen-Doped Carbon for the Electrocatalytic Synthesis of Hydrogen Peroxide. *J. Am. Chem. Soc.* **2012**, *134*, 4072–4075.
65. Sun, F.; Liu, J.; Chen, H.; Zhang, Z.; Qiao, W.; Long, D.; Ling, L. Nitrogen-Rich Mesoporous Carbons: Highly Efficient, Regenerable Metal-Free Catalysts for Low-Temperature Oxidation of H_2S. *ACS Catal.* **2013**, *3*, 862–870.
66. Kim, K. H.; Ihm, S. K. Heterogeneous Catalytic Wet Air Oxidation of Refractory Organic Pollutants in Industrial Wastewaters: A Review. *J. Hazard. Mater.* **2011**, *186*, 16–34.
67. Faria, P. C. C.; Órfão, J. J. M.; Pereira, M. F. R. Ozone Decomposition in Water Catalyzed by Activated Carbon: Influence of Chemical and Textural Properties. *Ind. Eng. Chem. Res.* **2006**, *45*, 2715–2721.
68. Gao, Y.; Hu, G.; Zhong, J.; Shi, Z.; Zhu, Y.; Su, D. S.; Wang, J.; Bao, X.; Ma, D. Nitrogen-Doped sp^2-Hybridized Carbon as a Superior Catalyst for Selective Oxidation. *Angew. Chem., Int. Ed.* **2013**, *52*, 2109–2113.
69. Figueiredo, J. L. Functionalization of Porous Carbons for Catalytic Applications. *J. Mater. Chem. A* **2013**, *1*, 9351–9364.
70. Cho, Y. J.; Kim, H. S.; Baik, S. Y.; Myung, Y.; Jung, C. S.; Kim, C. H.; Park, J.; Kang, H. S. Selective Nitrogen-Doping Structure of Nanosize Graphitic Layers. *J. Phys. Chem. C* **2011**, *115*, 3737–3744.
71. Bonvin, Y.; Callens, E.; Barrett, A. M. Bismuth-Catalyzed Benzylic Oxidations with *tert*-Butyl Hydroperoxide. *Org. Lett.* **2005**, *7*, 4549–4552.
72. Catino, A. J.; Forslund, R. E.; Doyle, M. P. Dirhodium(II) Caprolactamate: An Exceptional Catalyst for Allylic Oxidation. *J. Am. Chem. Soc.* **2004**, *126*, 13622–13623.
73. McLaughlin, E. C.; Choi, H.; Wang, K.; Chiou, G.; Doyle, M. P. Allylic Oxidations Catalyzed by Dirhodium Caprolactamate *via* Aqueous *tert*-Butyl Hydroperoxide: The Role of the *tert*-Butylperoxy Radical. *J. Org. Chem.* **2008**, *74*, 730–738.
74. Cornell, C. N.; Sigman, M. S. Discovery of and Mechanistic Insight into a Ligand-Modulated Palladium-Catalyzed Wacker Oxidation of Styrenes Using TBHP. *J. Am. Chem. Soc.* **2005**, *127*, 2796–2797.
75. Jeon, S. J.; Li, H.; Walsh, P. J. A Green Chemistry Approach to a More Efficient Asymmetric Catalyst: Solvent-Free and Highly Concentrated Alkyl Additions to Ketones. *J. Am. Chem. Soc.* **2005**, *127*, 16416–16425.